Flow paths in wetting unsaturated flow: Experiments and simulations

Eirik G. Flekkøy,[1] Jean Schmittbuhl,[3] Finn Løvholt,[2] Unni Oxaal,[2] Knut Jørgen Måløy,[1] and Per Aagaard[4]
[1]*Department of Physics, University of Oslo, P.O. Box 1048 Blindern, 0316 Oslo 3, Norway*
[2] *Landbrukshøyskolen på 1432 Ås, Ås, Norway*
[3] *Ecole Normale Supérieure, Rue Lhomond, 75005 Paris, France*
[4]*Department of Geology, University of Oslo, P.O. Box 1048 Blindern, 0316 Oslo 3, Norway*
(Received 20 September 2001; published 21 February 2002)

The flow paths and instabilities of gravity driven infiltration of a wetting fluid into a porous medium are studied. The model experiments and simulations independently represent techniques to study the unsaturated flow in porous media, and they produce a consistent picture of how the paths of fluid transport form and depend on the relative strength of the gravitational force. The experiments, which employ a transparent and quasi-two-dimensional model, reveal that the fluid pathways contain an internal link–blob structure and increase in width with decreasing gravity. The model, which couples the well established invasion percolation model for capillary governed flow with a model that describes the viscous film flow in partially filled pores, corroborates these experimental findings.

DOI: 10.1103/PhysRevE.65.036312 PACS number(s): 47.55.Mh

I. INTRODUCTION

Unsaturated flows govern a large number of environmentally important processes. The transport of pollutants from the soil surface to the ground water is governed by the slow transport through the unsaturated zone to the ground water table. The magnitude and evolution of this transport depends directly on the formation of fluid pathways. When the medium through which the transport takes place does not contain large scale heterogeneities the instabilities of the fluid flow itself are likely to select the structures through which the fluid flows. The typical case is where water (and possible water soluble contaminants) displaces air during its normally slow transport to the ground water table. Heterogeneities in sedimentary structures such as aquifers have many forms, such as channels formed by roots, or layers of coarser grains. However, one also finds relatively homogeneous sand deposits. The present paper focuses on such systems, and related cases where the hydrodynamic instabilities are not dominated by heterogeneities in the medium.

One of the most prominent features of the fluid structures are fingers of liquid that extend along the direction of gravity and show a remarkable persistence under variations in the flow conditions. These structures have been studied extensively in both quasi-two-dimensional (quasi:2D) [1] and quasi-three-dimensional [2,3] experiments. A theoretical understanding on the qualitative level has been reached to explain these experimental findings in terms of a gravitational version of the Saffman-Taylor instability [4,5].

Such flows have conventionally been modeled by the use of continuum equations [6,7], such as Richards equation, that take constitutive relations between capillary pressure and local saturation as well as between permeability and saturation [8–10], as input. It is at best unclear, however, if these models contain the physical ingredients necessary to capture the observed phenomena. In particular, it seems clear that the averaging procedures that produce constitutive relations in the form of one-to-one relationships cannot be given any general justification. Attempts to address these problems include models with improved multivalued constitutive relations. These are designed to incorporate effects of hysteresis on the level of the Richards equation [11].

In the present paper we focus experimentally and through simulations on two aspects of the fluid structures that form under unsaturated transport, the internal structure of the fingers and the finger width dependence on the bond number, i.e., the ratio of gravity and capillary forces. We observe that internally the fingers contain saturated regions that are surrounded by unsaturated regions. The finger width is observed to increase with the bond number.

The experimental model is transparent and consists of a monolayer of pores. This makes direct observation of the fluid structures possible, in contrast to earlier models where the pore to pore distribution of fluids have not been observed.

As the study introduces a pore-based model for the simulations the aim of the paper is also to validate this model. Contrary to macroscopic models, this model does not rely on the conventional approach via partial differential equations and constitutive relations. Instead, the present model relies on a microscopic picture of the porous media through which the fluid flows. For that reason, the model does not rely on macroscopic relations between permeability, capillary pressures, and saturation. The hysteretic effects, which are known to exist experimentally, follow as a result, rather than through *ad hoc* constitutive relations.

Pore network models similar to the one discussed here [12,13] as well as studies carried out with experimental network geometries [14] do exist. Compared to the existing simulation models the present model is enriched both with a description of the fluid pressure and the flow along films inside pore channels. Such flows are known to be important both from pore network experiments [13,14] and from experimental studies of thin film flow in fractures [15]. The present models describe the films by a continuous film thickness variable that evolves according to the capillary pressures and the viscosity. The film flow component of the model is then coupled to a migration component that de-

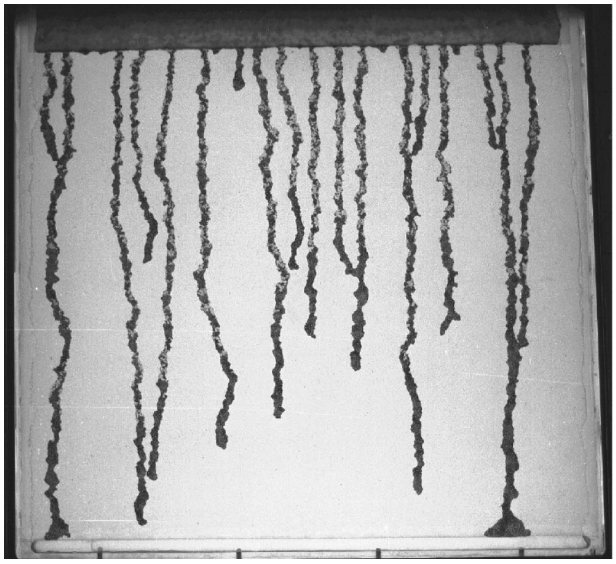

FIG. 1. The experiment at a tilt angle $\Theta = 90°$. The water, which is infiltrated from the top is dyed with black ink.

scribes the transport due to imbibition and drainage of pores.

II. THE EXPERIMENT

The experimental setup consists of a 63×63 cm^2 Hele-Shaw cell with a quasi-two-dimensional porous media, as shown in Fig. 1. The porous media is made by gluing a monolayer of glass beads between two sheets of contact paper. The sheets are then pressurized from the outside to prevent the paper and the beads from separating. On the top of the system there is a low permeability layer made of smaller beads. The large beads have a diameter of 1 mm$\pm$10%, and the small beads have a diameter of 0.3 mm$\pm$10%. The ink-colored water that is infiltrated from the top is supplied at atmospheric pressure, i.e., the water is not overpressured or underpressured. The whole experimental setup may be tilted in order to vary the magnitude of the effective gravitational pull on the water.

Since the present experimental model is transparent all the pore-scale structure of the invading fluid (water) is observable. This makes more details of the fluid structure directly observable. In particular, the experiment shows that the fingers are not without internal structure as previous observations may have indicated [4]. On the contrary, it is seen that the finger structures contain saturated islands linked by unsaturated regions.

The experiment is tilted at different angles to control the bond number

$$B = \frac{\rho g l^2}{\sigma}, \tag{1}$$

where σ is the surface tension, g the acceleration of gravity, and l a characteristic length scale. In the experiment, the tilting angle Θ has the effect $B \rightarrow B \sin(\Theta)$. In three-dimensional systems (that may not be tilted) this may correspond to either variations in the surface tension or the wetting properties of the medium.

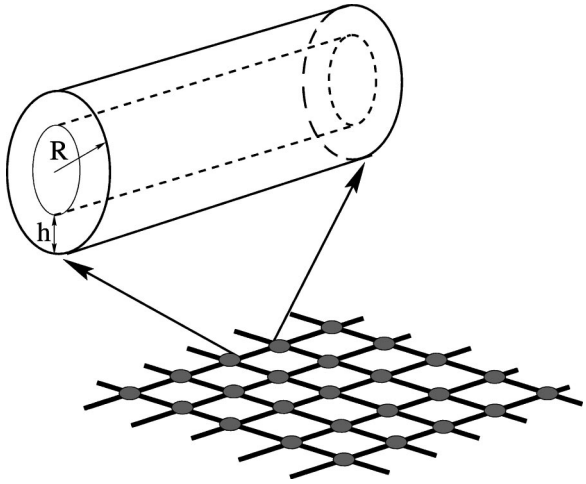

FIG. 2. The model description. The porous medium is represented as a 2D lattice of three-dimensional tubes. The fluid films are located on the inside of those tubes and evolve according to the interfaces shown here.

III. THE MODEL

The main simplification made in our modeling is illustrated in Fig. 2, which shows the discretization of the porous medium into a regular pipe network with variable channel radii R. This network could easily have been studied in three dimensions, and this is needed in many—but far from all real applications. In the context of the present quasi-2D experiments a two-dimensional description seems adequate.

In the experiments it is observed that the transport happens both through films in the unsaturated regions and through clusters of saturated pores. These clusters may move and thus transport the fluid inside them or stay at rest and form a medium for fluid flow through them. The present model seeks to describe all these transport processes within the geometry defined in Fig. 2. In this geometry the fluid may flow between the films on the walls of unsaturated pore channels or by drainage and imbibition processes as illustrated in Fig. 3.

Both natural and experimental porous geometries will typically exhibit a structure that causes the capillary pressures to fluctuate strongly with the positions of the fluid interfaces, even inside a single pore channel. This will generally cause strong hysteresis effects.

At the outset the geometric pore-scale structure in the model is that of cylinders. We will refine that structure by the introduction of different effective radii for drainage and imbibition, so that draining of a channel is associated with a larger capillary pressure drop than imbibition of the same channel. This is the experimental behavior seen, for instance, during imbibition/drainage of capillary tubes. It is also the only hysteretic effect we will introduce on the pore level. One among several possible physical mechanisms that gives rise to different effective drainage and imbibition radii R_D and R_I, is illustrated in Fig. 3. While the capillary pressure

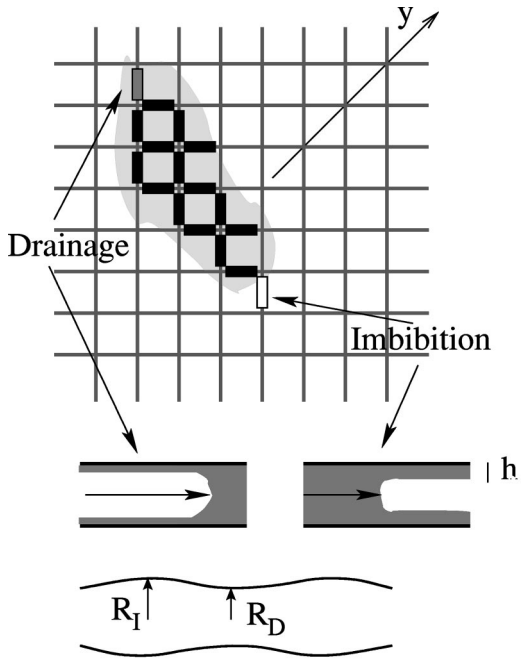

FIG. 3. Migrating droplet. In a single migration step the grey pore is drained while the white pore (imbibition) is filled, respecting volume conservation. The boundary of the droplet is used for the computation of the pressure difference.

determined by the widest part of the channel will be most important during an imbibition process, the opposite is generally true for a drainage process. This effect, which is sometimes called the ''ink bottle effect,'' as well as the capillary resistance associated with the passing of the pores connecting the channels are described by the difference between R_I and R_D. With these simplification stated it should be appreciated that the aim of the model is not to resolve details of the sub-pore-scale flow but rather the structures of the fluid transport on the scale above the pore scale.

A. The Film Flow

The model will be composed of two basic elements—one that describes the flow associated with the fluid interface configuration illustrated in Fig. 2 and one with the interfaces illustrated in Fig. 3.

Before we describe the migration steps illustrated in Fig. 3 we describe how the film flows in the unsaturated pores, and how the pressures in both saturated and unsaturated pores are determined.

The film flow part of the model describes the flow between unsaturated pores that is driven by the capillary forces (illustrated in Fig. 3) and gravity. It gives the changes in the film thickness h and the associated fluid pressure. The neighborhood that affects the film evolution in a pore channel is shown in Fig. 4. Here the film thicknesses h are used to compute the local capillary pressures $P=\sigma/(R-h)$ as well as the permeability. In general, the permeability of a channel will be given as a geometric factor of order unity times a squared length characteristic of the cross section of the channel. In the present case we will, for simplicity, take the geometric prefactor as unity and define the permeability $k=h^2$ [16]. The capillary pressure differences and gravity forces that drive the flow are computed from the middle of the pore channels, as shown in Fig. 4. Defining the volume flux from a pore along channel I_i as positive when the flux is directed outwards from the pore we may write Kirchhoff's law in the form

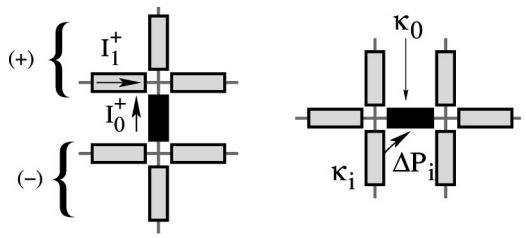

FIG. 4. The neighborhood of horizontal and vertical pore channels.

$$\sum_{i=1}^{3} I_i^{\pm} = -I_0^{\pm}, \tag{2}$$

where $I_0^{\pm}$ are the fluxes out of the pores labeled $\pm$ as shown in Fig. 4.

We need to relate the I_i's to the average flow velocity in a pore channel. Using that, this velocity takes place in a film of thickness h_i this relation takes the form $I_i=\pi(2R-h_i)h_i u_i$, where u_i is the flow velocity in pore channel i.

We introduce $P_i'=P_i-\rho g y_i$, where y_i is the depth of the center of the bond i measured from the top of the lattice and g is the acceleration of gravity. Note that the gravity is oriented along the diagonal of the lattice to avoid preferential directions resulting from the lattice geometry. Darcy's law in a channel takes the form $u_i=(k/\mu)\nabla P_i'$ where μ is the fluid viscosity. The pressure gradient may be estimated by the pressure difference between the pore and the center of the channel as $\nabla P_i' \approx 2(P_i'-P_x')/l$ where l is the channel length and P_x' is evaluated in the pore. Combining these results we may write the flux as

$$I_i=\kappa_i(P_i'-P_x') \tag{3}$$

where we have defined

$$\kappa_i=\frac{2\pi(2R_i-h_i)h_i k_i}{l\mu_0}. \tag{4}$$

Introducing the pressure drop between channel i and 0 $\Delta P_i'=P_i'-P_0'=P_i'-P_x'-(P_0'-P_x')$ we may use Eq. (3) to write

$$\Delta P'^{(+)}_i=\frac{I_0^{(+)}}{\kappa_0}-\frac{I_i^{(+)}}{\kappa_i^{(+)}}, \tag{5}$$

for the $(+)$ bonds shown in Fig. 4, and likewise for the $(-)$ side. The two contributions on the right-hand side correspond to the pressure drop through half of the neighboring channel i and half of the central channel 0. The acceleration

of gravity is g, $\Delta y_i = \pm l/\sqrt{2}$ is the depth difference between channels when lattice directions are 45° to the direction of gravity and ρ denotes the density of the fluid.

The fluid volume change in the pore channel 0 is given by

$$2\pi l(R_0 - h_0)\frac{dh_0}{dt} = I_0^{(+)} + I_0^{(-)}. \tag{6}$$

Multiplying Eq. (5) throughout by κ_i, summing over $i = 1, \ldots, 3$ and using the Kirchhoff's law we obtain

$$2\pi(R_0 - h_0)l\frac{dh_0}{dt} = I_0^{(+)} + I_0^{(-)} = \kappa_0 \frac{\sum_{i=0}^{3} \kappa_i^{(+)} \Delta P'^{(+)}_i}{\sum_{i=0}^{3} \kappa_i^{(+)}} + (+ \to -), \tag{7}$$

as the governing equation for the film evolution. Note that since $\Delta P'_0 = 0$ the sum runs from $i = 0$. A single update of the film is given by the explicit rule $h \to h + \dot{h}dt$.

1. The fluid pressure in full pores

What happens when the film thickness reaches the radius of the channel? Then the channel is full and no further film growth can occur. Physically the film is stopped from increasing its volume by pressure forces. These forces will allow flow through the channel but no net flow into or out of it.

In the model this mechanism is easily described by determination of the pressure P_0 that will cause $dh/dt = 0$ in Eq. (7). When a pore is full, i.e., when $h \geqslant R - \epsilon$, where ϵ is a small cutoff distance, we impose $\dot{h} = 0$. The result is that, while we describe the evolution of h in unsaturated regions we describe the evolution of the pressure in an incompressible liquid in the saturated regions. The boundary condition for this pressure solution is defined by the film pressures. The resulting pressures will be used in migration step that is described in the following section.

Setting $I = 0$ in Eq. (7) and inserting $\Delta P'_i = P_i - P_0 - \rho g \Delta y_i$ in Eq. (7) and solving for P_0 gives

$$P_0 - \rho g y_0 = \frac{\sum_{i=0}^{3} \kappa_i^{(+)}(P_i^{(+)} - \rho g y_i)}{2\sum_{i=0}^{3} \kappa_i^{(+)}} + (+ \to -), \tag{8}$$

where y_0 is the depth of bond 0. This equation should be considered an iteration equation that is applied to update P_0 at every saturated $(h = R)$ channel. Where there is a whole cluster of full pores, the pressure will adjust according to the capillary pressure values on the boundary of the cluster.

Equation (8) describes a set of linear equations. The difficulty is that the number of equations to solve evolves with time since the geometry of the incompressible fluid is always changing. We use and compare two solvers for computing the pressures P_i [17]: a relaxation technique that easily deals with moving boundaries but is weakly efficient and a conjugate gradient technique that is very efficient but requires care to incorporate the boundaries. The error was set to 10^{-6}. We checked that both techniques produce similar results.

2. Nondimensional form of the film equations

Both for the implementation of Eq. (7) and for comparison with experiments it is practical to take the dimensions out of this equation and identify the relevant dimensionless numbers. In order to do this we take the characteristic length to be the lattice constant l and the time T as the characteristic time it takes to fill a pore, i.e., $T \sim R/\dot{h}$. We may then define the dimensionless quantities

$$h' = \frac{h}{l}, \qquad t' = \frac{t}{T}, \tag{9}$$

and similarly for the other lengths in the problem, i.e., $R' = R/l$. Then Eq. (7) takes the form

$$\frac{dh'_0}{dt'} = C^{-1}\frac{\kappa'_0}{R'_0 - h'_0}\frac{\sum_{i=0}^{3} \kappa'^{(+)}_i \Delta \tilde{P}_i}{\sum_{i=0}^{3} \kappa'^{(+)}_i} + (+ \to -), \tag{10}$$

where

$$\tilde{P}_i = P'_i/(\sigma/l) = \begin{cases} \dfrac{1}{R'_i - h'_i} - By'_i & \text{where} \quad h' < R', \\ \dfrac{lP_{\text{inc}}}{\sigma} - By'_i & \text{where} \quad h' = R'. \end{cases} \tag{11}$$

and $y'_i = y_i/l$. Here the pressure P_{inc} is given by the volume conservation and the incompressibility condition described in the preceding subsection. We have also introduced the capillary number

$$C = \frac{\mu_0 l}{\sigma T}, \tag{12}$$

and bond number $B = \rho g l^2/\sigma$ as well as the dimensionless permeability function

$$\kappa' = (2R' - h')h'^3. \tag{13}$$

Note that the point of introducing the above dimensionless quantities is to identify the key dimensionless numbers, in this case C and B. These numbers, along with geometric ratios are the control parameters of the simulations, i.e., the above nondimensionless equations are used directly as the

basis of the simulations. This concludes the description of the film flow both for saturated and unsaturated pores.

B. Migration by invasion percolation

Figure 3 illustrates the migration step that consists in the combined imbibition (invasion) of one channel and drainage of another.

Physically, for a migration step to be possible, the threshold values of the capillary pressures in the two pores to be drained and imbibed must be exceeded. Now, when a channel (0) is imbibed there is contact between the fluid in that channel and the channels that are connected to it via the nearest node x (this will be one of the two nodes at the end of the channel). This means that we should compare P_0, P_x, and the capillary pressure. More precisely imbibition is possible if

$$P_x + \frac{\sigma}{R-h} > P_a, \tag{14}$$

where P_a is the air pressure and R is the radius of the imbibed channel. To get the pressure at site x we apply Kirchhoff's law on that site,

$$\sum_{i=0}^{3} \kappa_i (P_i - P_x - \rho g \Delta y_i) = 0. \tag{15}$$

Solving this equation for P_x and dividing by σ/l we obtain the nondimensional pressure on node x as

$$\tilde{P}_x = \sum_{i=0}^{3} \gamma_i^x (\tilde{P}_i - B\Delta y_i'), \tag{16}$$

where

$$\gamma_i^{\pm} = \frac{\kappa_i'^{\pm}}{\sum_{i=0}^{3} \kappa_i'^{\pm}}. \tag{17}$$

When a channel (0) is drained on the other hand, the fluid in it is replaced by air and will tend to lose contact with the other fluid from which it is displaced. This means that a drainage event will be governed by P_0, the air pressure P_a (if any) and the capillary pressures. More precisely, drainage is possible if

$$P_a - \frac{\sigma}{R_D} > P_0, \tag{18}$$

where P_0 is the pressure in the (saturated) channel to be drained.

Taking the dimension out by dividing by σ/l and setting $P_a = 0$ the imbibition and drainage conditions take the form

$$\Delta P_I = \tilde{P}_x + \frac{1}{R'-h'} > 0 \quad \text{for imbibition,}$$

$$\Delta P_D = \tilde{P}_0 + \frac{1}{R_D'} < 0 \quad \text{for drainage.} \tag{19}$$

The above criteria quantify when imbibition and drainage processes may start. However, since these processes are modeled as discrete events it is crucial that the criteria for them also guarantees completion. Otherwise, the process will overshoot and the simulations come to a halt because the fluid starts to bounce back and forth. The completion criteria are identified by noting that a downward proceeding drainage process or an upward proceeding imbibition process require larger driving forces to be completed than to be started, and they may, therefore, tend to stop halfway or when modeled as a discrete process, overshoot. The reason for this is the that both these processes are resisted by an increasing hydrostatic pressure component. In order to ensure that the initial driving pressures are sufficient to complete the process we must add these hydrostatic pressure components into the imbibition drainage criteria in the following way

$$\begin{aligned}
&\tilde{P}_x + \frac{1}{R'-h'} - \frac{B}{\sqrt{2}} > 0 \quad \text{for upward imbibition,} \\
&\tilde{P}_x + \frac{1}{R'-h'} > 0 \quad \text{for downward imbibition,} \\
&\tilde{P}_0 + \frac{1}{R_D'} < 0 \quad \text{for upward drainage,} \\
&\tilde{P}_0 + \frac{1}{R_D'} + \frac{B}{2\sqrt{2}} < 0 \quad \text{for downward drainage.}
\end{aligned} \tag{20}$$

The reason for the factor of 1/2 separating the correction factors of downward imbibition and upward drainage is the fact that P_0 is evaluated in the middle of a bond, while P_x is evaluated at a node. The criteria for upward imbibition and downward drainage contain no correction terms. Once these processes have passed the threshold to start they will also be completed.

When a cluster does not connect to any inlet the value of ΔP_D given by Eq. (19) must be used. If there exists an inlet, however, that supplies fluid at a given pressure P_0 the capillary pressure σ/R_D will not be felt. In this case ΔP_D must be calculated as $\Delta P_D = \tilde{P}_0 - P_n$, where P_n is the pressure in the channel neighboring the inlet.

For a migration step to occur, both ΔP_I and $-\Delta P_D$ must be positive. When this is the case for several channels simultaneously, the pair of channels that have the maximum values $\max(\Delta P_I)$ and $\max(-\Delta P_D)$ is chosen.

There is volume conservation so that the volume that is needed to fill a pore, and only that, is taken from the pore that is drained. The excess volume is left as a film in the drained pore. If the pore that is drained does not have sufficient volume to fill the imbibed pore, the drained pore is emptied and the imbibed pore receives the fluid as a film.

This will in general imply that this pore will be filled in the next migration step since $\sigma/(R-h)$ will just have increased.

C. Merging the migration and film flow

While the migration step is discontinuous and is carried out by an instantaneous motion of the fluid, the film flow is continuous in the sense that dt may be taken to be arbitrarily small. Physically of course, both processes take some time and ideally the migration steps and the film flow should be carried out in parallel at their physical speeds.

However, due to the way the migration step is implemented it must be carried out before or after the film flow step. The closest we can come to a parallel implementation is to invoke the film flow for a time Δt_F between each migration step. The problem is to associate a time Δt_M with each migration step. Then, by choosing $\Delta t_F = \Delta t_M$ the film will evolve for the same physical time as that corresponding to the migration step.

In principle, it is an easy matter to compute Δt_M since the pressure drops and local permeabilities κ define local speeds, and the volume of the pore channels are known. The time Δt_M may be taken as the volume to be filled in a drainage step divided by the volume flux. However, the pressures P that result from the film algorithm only characterizes the flow between—and not during—the migration steps.

Nevertheless, since the time of a migration step will be sensitive to the local pore geometries, and we have chosen to represent this geometry by highly simplified cylindrical channels, it makes no sense to attempt to obtain high-precision values of Δt_M. The lack of resolution on small spatial scales makes it natural to employ low resolution also at small time scales. On the basis of this modeling philosophy, we thus choose Δt_M as the time it would take to drain a pore at pressures frozen to have the values at the onset of the migration step. This leads to the formula

$$\Delta t_M = \frac{\mu l^2}{R^2 \min(\Delta P_D, \Delta P_I)}. \tag{21}$$

This result completes the definition of the model.

IV. RESULTS AND DISCUSSION

Given that several of the most significant findings of the present work, the structure and formation of the fingers, is of a qualitative nature we split the comparison between the simulations and experiments into a qualitative and a quantitative section. While important for validation purposes, the quantitative part of the results cannot be expected to carry over to real geological systems. The qualitative results, however, are likely to survive in more realistic settings, and we, therefore, place the main emphasis on them. For instance, the observation, both in simulations and experiments, that increasing B gives thinner fingers with a smaller fraction of saturated volume is expected to be robust. This implies that when pores become larger (thus increasing B) the fluid fraction becomes smaller and the transport more rapid.

Since the pore channels of the simulations do not correspond directly to the channels of the experiment the basic units of length are not directly comparable in the two cases.

Moreover, the experimental and simulated bond numbers are not directly comparable as they contain the microscopic length scale l. In the simulations l corresponds to the pore length, and in the experiments l is taken as the average bead size in the monolayer. However, since the microgeometry of the simulations is not intended to reproduce the experimental geometry there is an undetermined factor α between the bond number of the experiments and the simulations. We have chosen this factor according to the crossover to cluster formation observed both in the simulations and experiments. The value of B where this happens depends on R_D/R, and the factor α is chosen so the rescaled experimental B agrees with the bond number used in the simulations at the point where the crossover takes place when $R_D/R = 0.6$. In the following, it is this rescaled experimental bond number that is used. In all simulations there was an initial film thickness $h = 0.01R$ and they were carried out at different R/R_D, C, and B.

In real systems, the present experiments included, not only the value of R/R_D but the variance of R_D is an important parameter. Typically the root of the variance in R_D will be of the same order as R_D itself. For simplicity, however, we have chosen to perform the simulations with a the root of the variance in R_D of 0.1% of R_D. The finite but very small value was chosen in order to avoid potential artifacts resulting from having absolutely no noise at all.

A. Qualitative comparison

To carry out the simulations in the relevant parameter regime we have chosen a ratio of the top to bottom layer pore radii of 3.5. This corresponds to the experimentally measured permeability contrast $\kappa_{bottom}/\kappa_{top} = 3.5^2$. The capillary number C was set to 0.1, which is of the same order of magnitude as in the experiments. However, the results showed only a very weak dependence on C around 0.1.

The fingering structures and their characteristics observed by Glass and Parlange, are reproduced here. This is shown in Fig. 1.

Figure 5 also shows the internal structure of the fingers. The dark regions are saturated whereas, the regions that connect them are not.

Figure 6 shows a time sequence during an infiltration simulation. The main point of this figure is to show the structure of the saturated clusters that form behind the advancing finger tip. Once these clusters are formed they remain stationary even though fluid is moving through them as the finger is growing. This is exactly what is observed in the experimental image, Fig. 5, as well.

Figure 7 shows how the width and structures of the fingers change with B in the experiments. Simulations designed to match Fig. 7 were carried out, and the finger widths measured as a function of B. In the simulations the finger width was measured simply as the number of full bonds in a finger divided by the finger length. In the experiments the widths were obtained by direct measurement on the images. The widths were measured by a ruler at a sequence of different

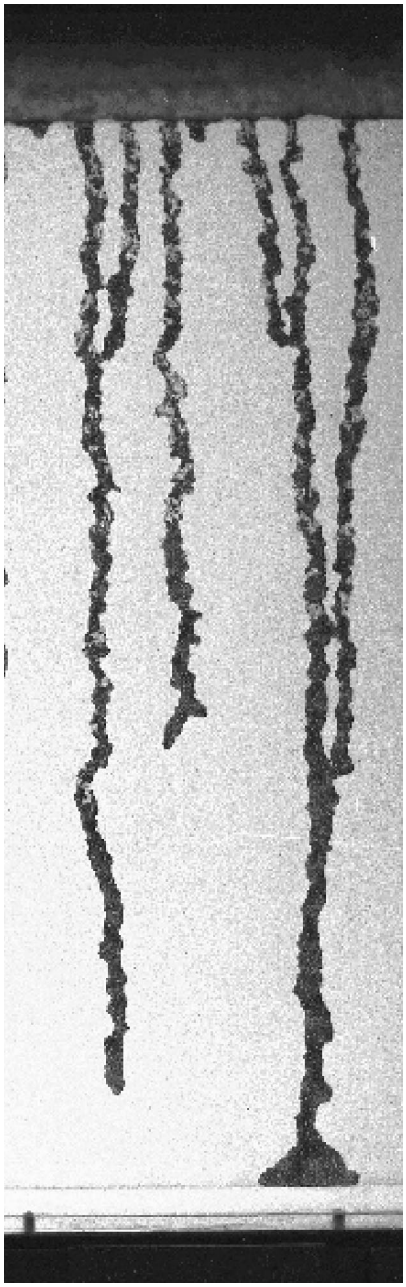

FIG. 5. A detailed 20-by-63-cm section of the $\Theta = 90°$ experiment of Fig. 1 showing the internal blob structure of the fingers.

heights and then averaged. The uncertainty in both cases is the characteristic variance of the width.

Figure 8, which should be compared with Fig. 7, shows fluid configurations resulting from different B. As in the experiments, the fingers become thicker with decreasing B. Also the crossover to fingers consisting of saturated clusters are reproduced by the simulations. For $R_D/R = 0.4$, the crossover value of B is approximately 0.05. For larger R_D/R the crossover B becomes smaller. As B is increased both simulations and experiments show a decreasing cluster size, and in both cases the length of the finger tip is substantially longer than the internal clusters. This is caused by the fact that imbibition into an already wet pore happens more easily than the imbibition into an almost dry pore.

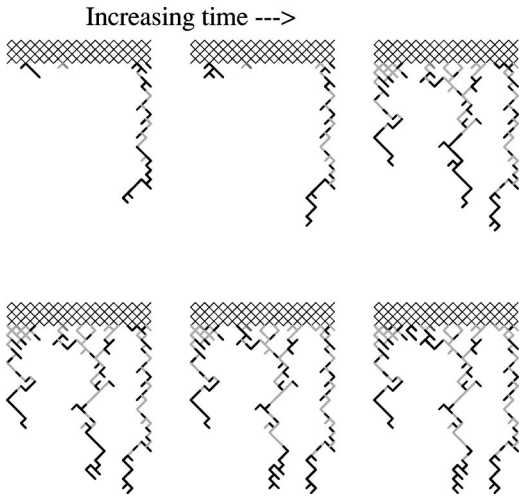

FIG. 6. Snapshots of infiltration simulations at different times for $B = 0.20$ and $R_D/R = 0.6$. Black bonds are saturated while unsaturated bonds are shown in gray. Light gray corresponds to small film thicknesses and dark gray to large thicknesses.

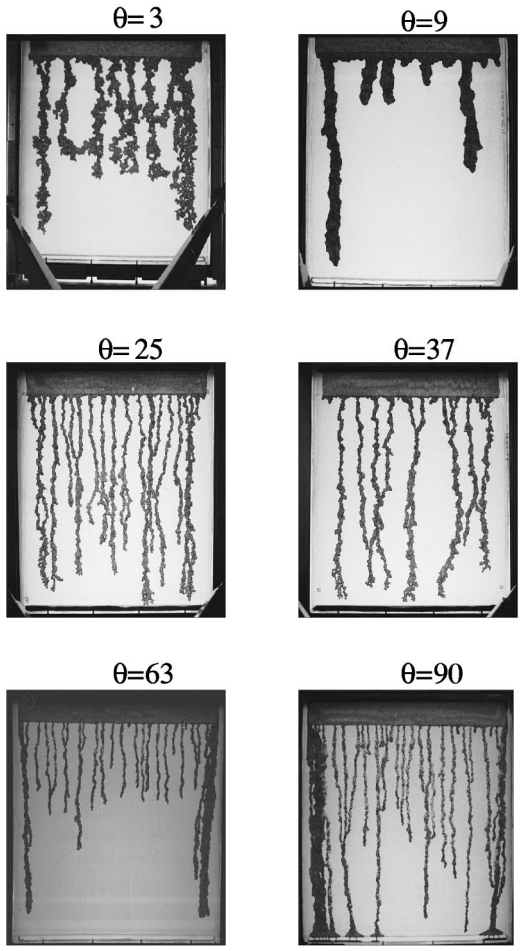

FIG. 7. Experiments at different B given by the tilt angle Θ to the vertical.

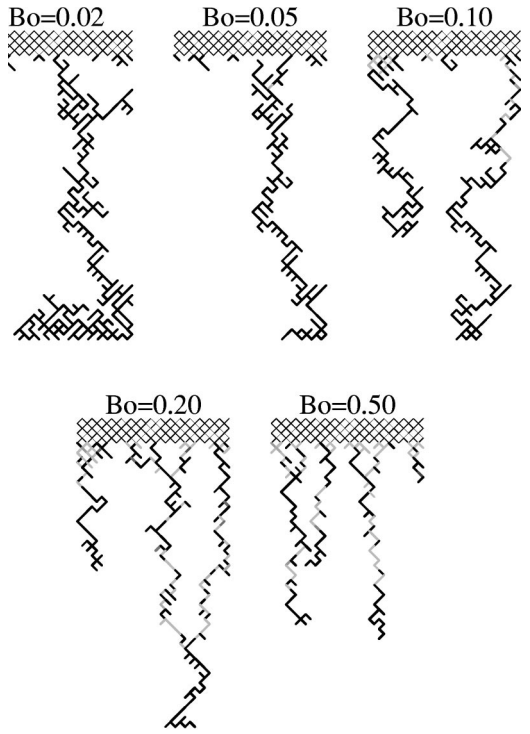

FIG. 8. Snapshots of infiltration simulations at different B for $R_D/R=0.4$. The color coding is as in Fig. 6.

Note the merging of two fingers in the $B=0.20$ and $B=0.50$ snapshots. In the simulations, as in the experiment, fingers merge but do not show tip splitting.

B. Towards a quantitative comparison

In the following we will obtain and compare three different lengths, the average finger diameters d the average length of the saturated finger tip l, and the average distance Δs between fingers. The natural length scale in the system with which to normalize these lengths is the height of the top layer H. This is the scale we will use both for the experimental and simulated results.

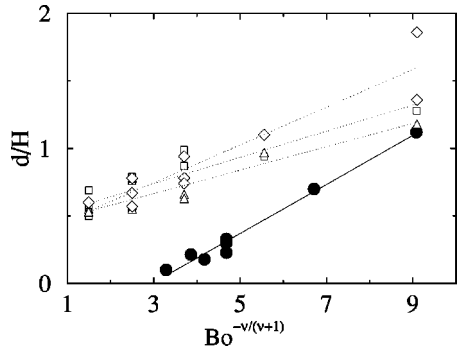

FIG. 9. The average finger diameter d (normalized by H, the thickness of the top layer) as a function of $B^{-\nu/(\nu+1)}\approx B^{-0.57}$, where ν is the correlation length exponent of invasion percolation. The experimental values (●) are fitted with a black line and the simulations with gray lines. The different simulations correspond to $R_D/R=0.4$(□), 0.6(△), and 0.8(◇).

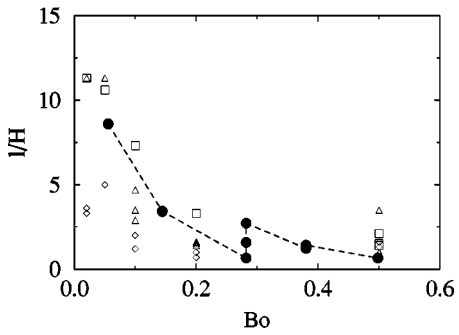

FIG. 10. The average length l of the saturated tip of the fingers (normalized by H, the thickness of the top layer). The experimental values (●) are connected by a dashed line and the open symbols correspond to simulations with $R_D/R=0.4$(□), 0.6(△), and 0.8(◇).

Figure 9 shows the average finger diameter as a function of $B^{-\nu/(\nu+1)}$, where ν is the correlation length exponent of invasion percolation [18]. This particular scaling ansatz is motivated by the idea that on short length scales the structure of fluid clusters are given by the invasion percolation algorithm [18], and that this structure is modified by gravity only at scales larger than a gravitational length given by B.

It is observed that both simulations and experiments are consistent with the $d/h\sim B^{-\nu/(\nu+1)}$ behavior over the limited range of B explored. However, this agreement is only suggestive, not conclusive. The constant of proportionality between d/h and $B^{-\nu/(\nu+1)}$ is expected to depend on pore-scale details and varies between experiments and simulations, and also between simulations with different values of R_D/R. Figure 10 shows the behavior of the length l of the saturated finger tip with bond number. It is observed that the values $R_D/R=0.4$ and 0.6 reproduce the experimental behavior more closely than $R_D/R=0.8$.

Finally, we compare the experimental and simulated values of the average spacing between the fingers (Fig. 11). This measurement as well is marked by a significant amount of noise as in the simulations only one to five or six fingers appeared and in the experiments the number of fingers varied rather strongly even for fixed B. The (○)'s results from the

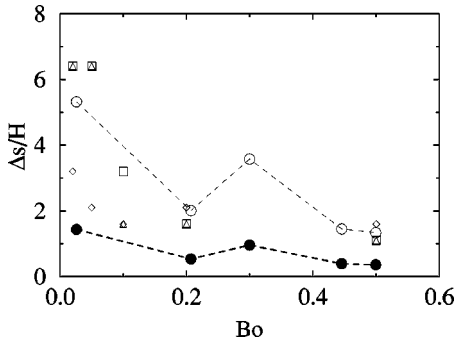

FIG. 11. The average spacing Δs between fingers (normalized by H, the thickness of the top layer) as a function of B. The symbols used are the same as in Fig. 10. The experimental data shown by (○)'s connected by a dashed line are the same as those shown by (●), but the normalization is changed as $H\rightarrow H/3.8$.

data shown by the (●)'s by a common rescaling by a factor 3.8. It may thus be observed that only the general scaling behavior is consistent between the simulations and experiments. This may be linked to the differences in the hydrodynamic coupling between the top and bottom layers in the experimental and numerical models. The quantities Δs and l depend rather strongly on R_D/R. The width d has a much weaker R_D/R dependence. This quantity is a geometric characterization of the microscopic pore structure, and it will typically have large natural fluctuations. In real geological systems these fluctuations will not be easily quantified or predicted. Hence, when the model is applied to say something about such real systems, simulations of different R_D/R will provide an estimate of the variability due to pore-level fluctuations rather than exact predictions.

V. CONCLUSIONS

Having carried out both experiments and simulations to investigate the structure of the fluid pathways, we note a few main findings. Theoretical considerations indicate that it is the bond number B and capillary number C that constitute the control parameters of the system besides the numbers characterizing the geometry. The simulations are carried out to model, support, and compliment the experiments, and the focus of the computational effort has mainly been to demonstrate that the key physical features put into the model reproduce the main *qualitative* findings of the experiments.

These are discussed as follows. When B is increased (by increasing gravity or the pore size) fingers become thinner, and more closely spaced. This has been observed previously [4]. What is different in the present work is the observed blob–link structure in the fingers. These structures, a large blob at the advancing finger tip, and smaller blobs behind it, are strikingly robust under the fluid flow. The existence of these structures demonstrates that less water is present in the vadose zone than would appear from the mere existence of fingers. However, this is true only above a critical bond number. When B is below the critical value the fingers become saturated throughout their length. It is also observed that while fingers may merge, they do not split. Since the fingers appear to move randomly in the horizontal direction this indicates that the number of fingers will decrease steadily with depth. All these qualitative observations are made both in the simulations and experiments.

On the quantitative side, the agreement is less striking, mostly owing to the fact that these measurements depend on pore-scale details of the porous media, features that are not sought or captured in the simulations. However, we showed that the diameter of the finger decreases with the bond number (i.e., gravity). A consistent fit of this evolution is given by the invasion percolation estimate $d/h \propto B^{-\nu/(\nu+1)}$. We also show that the average length of the fingers significantly decreases with the bond number. Finally, we studied the spacing between fingers and obtained a decrease of this spacing when increasing the bond number, that is, a higher density of fingers when gravity is increased. Numerical and experimental results are in good agreement in terms of parameter sensitivity.

[1] R. J. Glass, T. S. Steenhuis, and J.-Y. Parlange, Water Resour. Res. **25**, 1195 (1989).

[2] R. J. Glass, S. Cann, J. King, N. Baily, J.-Y. Parlange, and T. S. Steenhuis, Transp. Porous Media **5**, 247 (1990).

[3] R. J. Glass, J.-Y. Parlange, and T. S. Steenhuis, Water Resour. Res. **27**, 1947 (1991).

[4] R. J. Glass, T. S. Steenhuis, and J.-Y. Parlange, Soil Science **148**, 60 (1989).

[5] P. G. Saffman and G. Taylor, Proc. R. Soc. London, Ser. A **245**, 312 (1958).

[6] P. A. C. Raats and A. Klute, Soil Sci. Soc. Am. J. **32**, 161 (1968).

[7] P. A. C. Raats and A. Klute, Soil Sci. Soc. Am. J. **32**, 452 (1968).

[8] T. J. Marshall, J. Soil Sci. **9**, 1 (1958).

[9] R. H. Brooks and A. T. Corey, Report, 1964 (unpublished).

[10] M. Th. van Genuchten, Soil Sci. Soc. Am. J. **44**, 892 (1980).

[11] P. Lehmann, F. Stauffer, C. Hinz, O. Dury, and H. Fluhler, J. Contam. Hydrol. **33**, 81 (1998).

[12] E. Aker, K. J. Måløy, A. Hansen, and G. G. Batrouni, Transp. Porous Media **32**, 63 (1998).

[13] G. G. Pereira, W. V. Pinczewski, D. Y. C. Chan, L. Paterson, and P. E. Øren, Transp. Porous Media **24**, 167 (1996).

[14] R. Lenormand, C. Zarcone, and A. Sarr, J. Fluid Mech. **135**, 337 (1983).

[15] T. K. Tokunaga and J. Wan, Water Resour. Res. **33**, 287 (1997).

[16] L. D. Landau and E. M. Lifshitz, *Fluid Mechanics* (Pergamon Press, New York, 1959).

[17] W. H. Press, S. A. Teukolsky, W. T. Vetterling, and B. P. Flannery, *Numerical Recipes* (Cambridge University Press, Cambridge, 1992).

[18] D. Wilkinson and J. F. Willemsen, J. Phys. A **16**, 3365 (1983).